**J. Cent. South Univ.** (2022) 29: 871−882
**DOI:** https://doi.org/10.1007/s11771-022-4962-4

Springer

# Microstructure and mechanical properties of friction stir welded powder metallurgy AA2024 alloy

HAN Wei-hao(韩未豪)[1], LI Pei(李沛)[1], LIU Nan(刘楠)[2], CHEN Cun-guang(陈存广)[1, 3, 4]*, DONG Shi-peng(董诗鹏)[1], GUO Zhi-meng(郭志猛)[1, 4], YANG Fang(杨芳)[1, 4], SUI Yan-li(隋延力)[3, 4], VOLINSKY Alex A[5]

1. Institute for Advanced Materials and Technology, University of Science and Technology Beijing, Beijing 100083, China;
2. Beijing Engineering Research Center of High Purity Metal Sputtering Target, Beijing 102200, China;
3. State Key Laboratory for Advanced Metals and Materials, University of Science and Technology Beijing, Beijing 100083, China;
4. Innovation Group of Marine Engineering Materials and Corrosion Control, Southern Marine Science and Engineering Guangdong Laboratory (Zhuhai), Zhuhai 519082, China;
5. Department of Mechanical Engineering, University of South Florida, Tampa, Florida 33620, USA



**Abstract:** The extruded plate of powder metallurgy AA2024 aluminum alloy was successfully solid-state joined by friction stir welding (FSW) to demonstrate potential applications in the aerospace and automotive industries. For determining the optimal processing parameters of FSW, the microstructure, mechanical properties, and fracture behavior of FSW joints were evaluated. When the processing parameters were optimized with 2000 r/min rotation speed and 100 mm/min traverse speed, high quality welds were achieved. The ultimate tensile strength yield strength and elongation of the joint can reach 415 MPa (85% of the base metal strength), 282 MPa, and 9.5%, respectively. The hardness of the joint gradually decreased from the alloy matrix to the heat-affected zone. The lowest strength and hardness appeared near the heat-affected zone because of the over-aging caused by heat flow from repeated stirring during FSW. The average grain size of the stir zone (2.15 μm) was smaller than that of the base metal (4.43 μm) and the heat-affected zone (5.03 μm), whose grains had <110> preferred orientation.

**Key words:** high-strength aluminum alloy; powder metallurgy; AA2024 alloy; friction stir welding; mechanical properties

**Cite this article as:** HAN Wei-hao, LI Pei, LIU Nan, CHEN Cun-guang, DONG Shi-peng, GUO Zhi-meng, YANG Fang, SUI Yan-li, VOLINSKY Alex A. Microstructure and mechanical properties of friction stir welded powder metallurgy AA2024 alloy [J]. Journal of Central South University, 2022, 29(3): 871−882. DOI: https://doi.org/10.1007/s11771-022-4962-4.

**Foundation item:** Project(92066205) supported by the National Natural Science Foundation of China; Project(JCKY61420052008) supported by the National Defense Science and Technology Key Laboratory Foundation, China; Project(311021013) supported by Innovation Group Project of Southern Marine Science and Engineering Guangdong Laboratory (Zhuhai), China; Project(FRF-MP-20-52) supported by the Fundamental Research Funds for the Central Universities, China; Project(075-15-2021-612) support from the Government of the Russian Federation

**Received date:** 2021-06-30; **Accepted date:** 2021-10-20

**Corresponding author:** CHEN Cun-guang, PhD, Research Assistant; Tel: +86-10-62334341; E-mail: cgchen@ustb.edu.cn; ORCID: https://orcid.org/0000-0002-6525-228X

## 1 Introduction

High-strength aluminum alloys with refined microstructure and fine reinforcement particles fabricated by powder metallurgy (PM) have attracted attention as novel lightweight structural materials for applications in the automotive, aerospace, military, and marine industries [1 − 5]. Particularly in the automotive field, PM high-strength aluminum alloys are in a greatest demand to improve energy efficiency and reduce emissions. On the one hand, vehicle components can be produced from sintered aluminum alloys, such as AC2014 (Al-4.4Cu-0.8Si-0.6Mg) with reasonable mechanical properties, offering the combination of weight and material savings due to the low density and near net shape processing [6, 7]. To broaden aluminum PM technology applications, considerable research efforts have emphasized the development of large-size sintered billets of high-strength aluminum alloys. For example, PM AA2024 and PM AA7055 can be made into bars, profiles, and plates by plastic deformation [8 − 10]. However, it is challenging to joint or assemble PM high-strength aluminum alloys applied in manufacturing engineering and industrial complex structures, because the reinforcing $Al_2O_3$ nanoparticles together with precipitated phases ($Al_2Cu$, $Al_2CuMg$, $MgZn_2$, etc.) tend to agglomerate and may produce cracks in the joints [11−13].

To date, friction stir welding (FSW) has demonstrated significant promise as a solid-state joining technique for metals [14 − 18] and composites [19 − 24]. In effect, PM high-strength aluminum alloys can be also considered as aluminum-matrix nanocomposites due to the dispersion strengthening mechanism of $Al_2O_3$ nanoparticles, namely oxide dispersion strengthened (ODS) aluminum alloys [25 − 27]. The fusion welding processes, including gas metal arc welding, usually result in transport and agglomeration of the finely dispersed oxides on the surface of the weld pool, thereby degrading the joint strength. FSW has incorporated oxide particles into the metal matrix to produce ODS copper and steel [28, 29]. Several studies have shown that the fine distribution of $Al_2O_3$ nanoparticles in the pure aluminum matrix by FSW is feasible [30−32].

Multiple papers in the past few years have emphasized the preparation of powder metallurgy high-strength aluminum alloys [8, 25, 33, 34]. However, the results of PM high-strength aluminum alloys FSW processing have not been reported yet. This work aims to study the microstructure, mechanical properties, and fracture behavior of the FSW PM AA2024 aluminum alloy. The plate of PM AA2024 alloy was fabricated by a powder metallurgy route and subsequent hot extrusion, and the effects of FSW processing parameters on the weldability of the material were studied. After establishing a suitable working window, the microstructure, microhardness, and tensile properties of the welds were evaluated.

## 2 Experimental

The chemical composition of PM AA2024 aluminum alloy used in this study is Cu 4.74 wt.%, Mg 1.73 wt.% , and Al in balance. The primary billets with 203 mm diameter were prepared by powder metallurgy, which included powder mixing, cold isostatic pressing, and sintering, as reported in detail elsewhere [8]. Subsequently, the sintered ingots were hot extruded into 50 mm thick and 137 mm wide plates, with the extrusion ratio of 5:1 at 405 °C. The plates were heat-treated at 490 °C for 2 h, quenched in water at room temperature, and naturally aged at room temperature for 7 d (T4 heat treatment).

The PM 2024-T4 aluminum alloy plates were machined (wire cut and milled) to the dimensions of 100 mm (length)×60 mm (width)×3 mm (thickness), and joined by FSW. Figure 1(a) shows the FSW process schematics, including rotating and travel directions. The longitudinal direction (also known as the welding direction, WD) of the plates is perpendicular to the extrusion direction (ED), and normal direction (thickness direction, ND). The diameters of the shoulder and cylindrical pin were 10 mm and 3 mm, respectively, and the length of the pin was 2.85 mm. To determine the optimal process parameters, FSW trials were performed at the traverse speed $v$ of 40−120 mm/min and the rotation speed $\omega$ of 1000 − 2000 r/min. Specific parameters are listed in Table 1.

Microstructure examinations of the welded joints were carried out by scanning electron

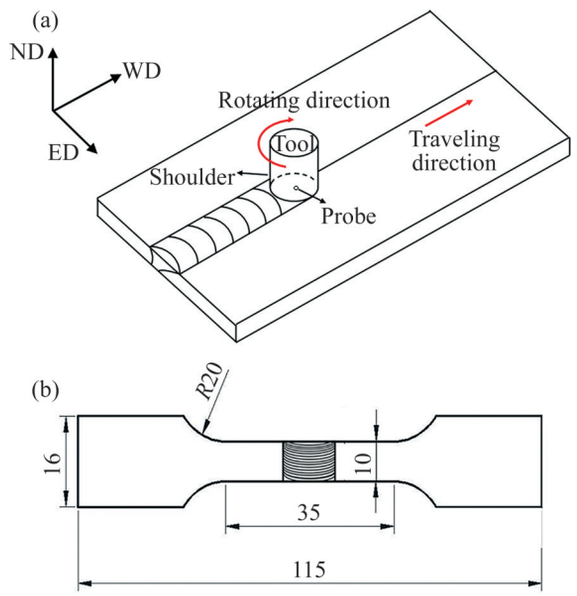


**Figure 1** (a) Illustration of the friction stir welding process; (b) Geometry of the tensile sample with a weld (Unit: mm)

microscopy (SEM, LEO 1450, Carl-Zeiss) at 20 kV, field-emission scanning electron microscopy (FE-SEM, SUPRA 55, Carl-Zeiss) at 15 kV, and electron backscatter diffraction (EBSD, SUPRA 55, Carl-Zeiss) at 20 kV. The distribution of the secondary phases was analyzed by an energy dispersive spectrometer (EDS). To evaluate the mechanical properties of the welds, tensile tests were performed at room temperature at 0.5 mm/min speed. The tensile specimens were cut from the center of the plate with the weld in the middle of the sample length, as shown in Figure 1(b). The dog-bone-shaped samples were 10 mm wide, 3 mm thick, and 115 mm long. Vickers micro-hardness along the joints cross-section was measured with 50 g load and 0.5 mm spacing between indentations. Two sets of micro-hardness measurements were carried out from the top to the bottom on the cross-section of the joints.

## 3 Results and discussion

### 3.1 Optimal FSW parameters

The FSW process parameters include the rotation and the traverse speed, which have important effects on joint forming. The welding heat input directly affects the plastic flow of the material and the temperature of the welding nugget. The heat input, $q_E$, in the welding process can be calculated as:

$$q_E = \frac{\pi\mu\omega P\left(r_0^2 + r_0 r_1 + r_1^2\right)}{45\left(r_0 + r_1\right)v} = k\frac{\omega}{v} \quad (1)$$

According to Eq. (1), the welding thermal input $q_E$ is proportional to the ratio of the rotation speed to the traverse speed $\omega/v$, which can be used as a standard to measure the thermal input in the welding process. The FSW parameters used in this work and the corresponding mechanical properties of the welded joints are listed in Table 1.

Figure 2 shows the surface morphology of PM 2024 aluminum alloy welds obtained using different welding parameters. Figures 2(b) and 2(e) show macroscopic defects in the welded joints of samples 2 and 5. The reason for defects is that the thermal input during FSW is inadequate ($\omega/v$=12.5), leading to low temperature in the joint area, insufficient degree of stirring, and poor metal plastic flow. Eventually, the accumulation of the plastically

**Table 1** Mechanical properties of PM AA2024 with different FSW parameters

| Sample | $\omega$/(r·min$^{-1}$) | $v$/(mm·min$^{-1}$) | $\omega/v$ | UTS/MPa | YS/MPa | Elongation/% | Joint coefficient/% |
|---|---|---|---|---|---|---|---|
| BM | — | — | — | 476 | 326 | 17.0 | — |
| 1 | 1000 | 40 | 25.0 | 287 | 246 | 3.0 | 60 |
| 2 | 1000 | 80 | 12.5 | 251 | 246 | 2.0 | 53 |
| 3 | 1500 | 40 | 37.5 | 305 | 252 | 2.7 | 64 |
| 4 | 1500 | 80 | 18.7 | 330 | 276 | 2.5 | 70 |
| 5 | 1500 | 120 | 12.5 | 253 | 246 | 2.0 | 53 |
| 6 | 1800 | 40 | 45.0 | 310 | 243 | 4.0 | 65 |
| 7 | 1800 | 80 | 22.5 | 340 | 267 | 3.0 | 72 |
| 8 | 2000 | 80 | 25.0 | 337 | 274 | 4.0 | 71 |
| 9 | 2000 | 100 | 20.0 | 415 | 282 | 9.5 | 85 |

Annotation: Joint coefficient means the ratio of the UTS of the welded joint to UTS of the base metal.

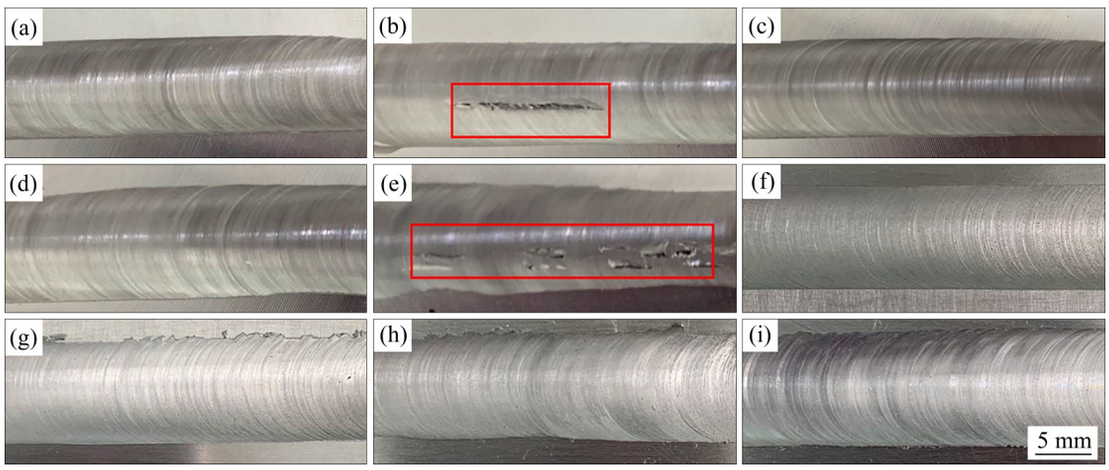


**Figure 2** Macroscopic features of friction stir welding joints using different welding parameters: (a−h) Samples 1−9 in Table 1

deformed metal lessens, and the weld cannot be completely filled, resulting in surface defects such as furrows and holes. No obvious macroscopic defects were found in other samples.

The relationship between the thermal input and the joining performance is shown in Table 1 and Figure 3. The ultimate tensile strength (UTS) and yield strength (YS) of FSW joints first increase and then decrease with the $\omega/v$ ratio, and there is an optimal ratio. When $\omega/v$=12.5 for samples 2 and 5, the mechanical properties of the welded joints are the worst, with the 251−253 MPa of UTS, 246 MPa of YS, and 2% of elongation. The loss ratio of the joint strength reaches up to 47%. The optimal mechanical properties of the joint of sample 9 are achieved at $\omega/v$ =20, with 415 MPa of UTS, 282 MPa of YS, and 9.5% of elongation. The joint efficiency of the sample 9 is 85% in terms of the

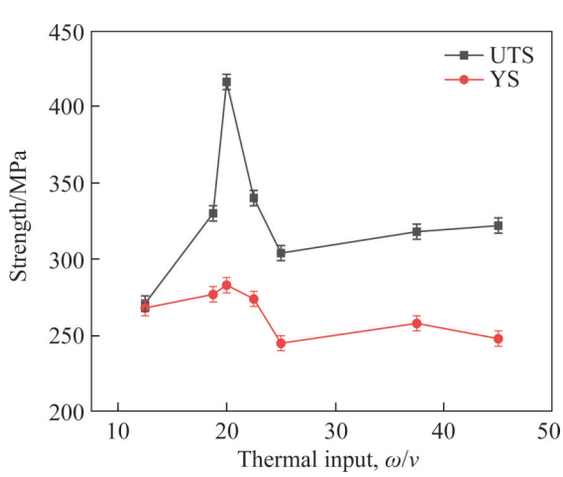


**Figure 3** Strength of friction stir welding joints as a function of welding thermal input

UTS. The mechanical performance of the FSW joints varies with the welding heat input, and is related to metal accumulation and the grain size increases in the stir welding zone. High welding heat input will lead to excess heat accumulation of metals, resulting in grains coarsening in the stir welding zone, weakening the joint performance. On the other hand, insufficient heat input results in less metal accumulation, and poor fluidity. When the plastic metal cannot reach the position of the hole in time under high welding speed, it is easy to form holes and other defects, which adversely affect mechanical properties of the joint.

### 3.2 FSW joint microstructure

Generally, FSW produces four kinds of distinct microstructure zones, namely the stir zone (SZ), thermo-mechanical affected zone (TMAZ), heat-affected zone (HAZ), and base metal (BM). Figure 4 shows that the FSW joint in this work is mainly composed of the SZ, TMAZ, HAZ, and BM. According to the relative direction of the traverse speed and rotation speed, the TMAZ can be divided into advancing side thermo-mechanical affected zone (AS-TMAZ) and retreating side thermo-mechanical affected (RS-TMAZ). In the welding process, the pin tool rotates counterclockwise. One side of the weld in the direction of the advancing tool pin is the advancing side. The opposite side is the retreating side. As seen in Figure 4, since the relative velocity of the advancing side is higher than the retreating side in the welding process, the shear force induced by the advancing tool pin of the metal

is higher in the welding process, so the boundary between the weld zone on the AS-TMAZ is more obvious than RS-TMAZ.

The grains morphology, size, and orientation distribution of each region of the joint are significant factors noticeably influencing the mechanical properties of the joint. Therefore, EBSD was carried out on each region of the joint to analyze the microstructure evolution. Figures 5 and 6 show the grain orientation maps (OIMs) and grain size distribution of each area of the FSW joint, determined by EBSD and analyzed by the Channel 5 software integrated into the ZEISS SUPRA™ 55 SEM. Due to the BM formed by extrusion and T4 heat treatment before welding, grains in BM are stretched along the ED into fibers, as seen in Figure 5(e). The grains preferred orientation in BM is along the <110> direction, while a few grains are oriented along the <001> direction. According to calculations, the average grain size of the BM is 4.43 μm. Figure 5(b) shows that the equiaxed grain structure in SZ replaces the original elongated grain


**Figure 4** Optical macrograph of friction stir welding joint cross-section

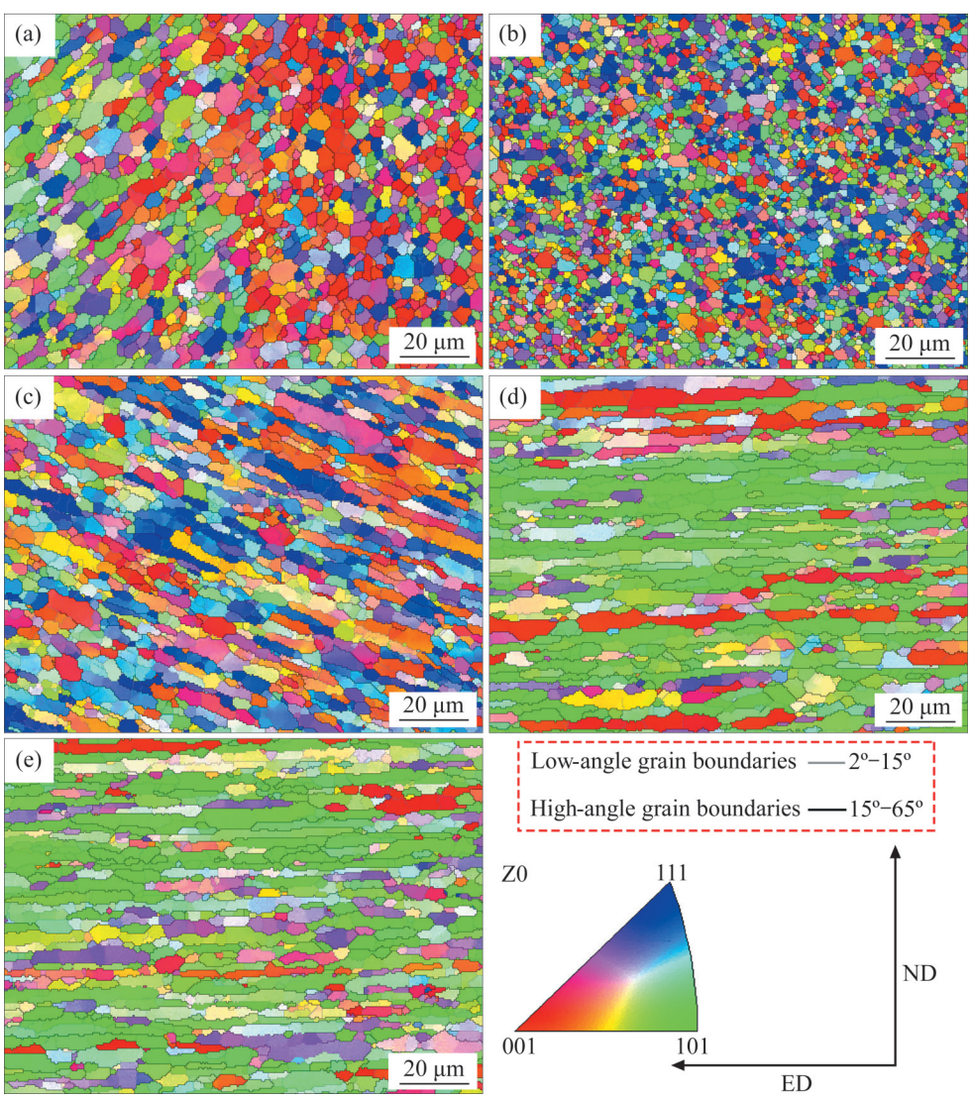


**Figure 5** Grain orientation maps of (a) AS-TMAZ, (b) SZ, (c) RS-TMAZ, (d) HAZ and (e) BM of the friction stir welding joints

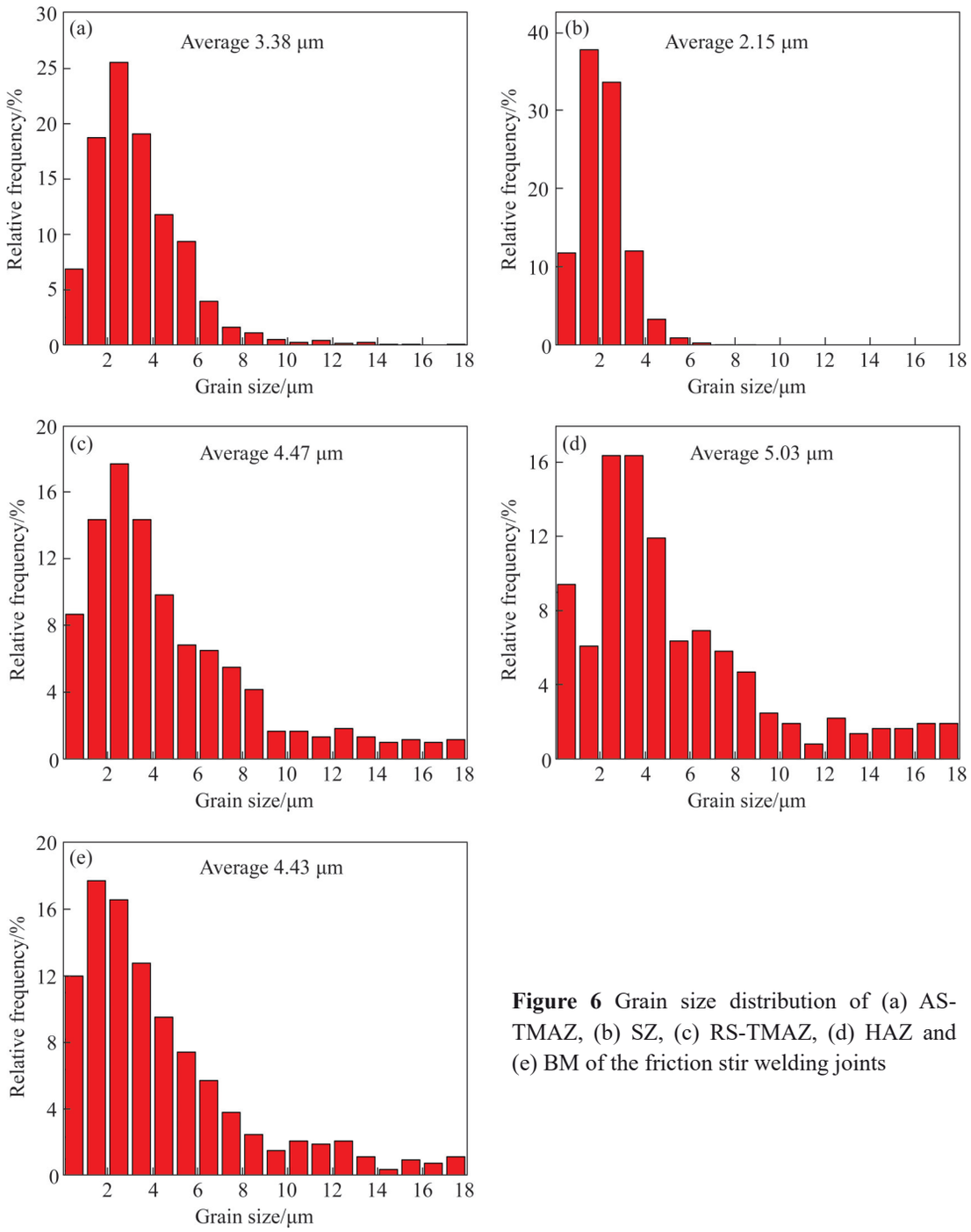


**Figure 6** Grain size distribution of (a) AS-TMAZ, (b) SZ, (c) RS-TMAZ, (d) HAZ and (e) BM of the friction stir welding joints

in BM, with an average grain size of 2.15 μm. The fine recrystallized microstructure is obtained due to the broken grains and the high temperature in the weld. Figures 5(a) and (c) show that equiaxed grains can be found in the TMAZ, but the grain size is larger than the SZ, because of the weaker stirring effect in TMAZ. The average grain size of AS-TMAZ and RS-TMAZ is 3.38 μm and 4.47 μm, respectively.

As is well known, the HAZ is generally the weakest fracture location, so it is necessary to focus on the analysis of the HAZ structure. The grain morphology and grain orientation distribution of HAZ is similar to BM, that is, the grains are still elongated and the grain size of HAZ is similar to BM. The direction of the optimal orientation is <110 >. This is because HAZ is far away from the weld, and there is no significant plastic deformation. At the same time, it is affected by the welding thermal cycle, so the grains grow after heating. According to

statistical analysis, the average grain size in the heat-affected zone is 5.03 μm, which is 12% larger compared with BM.

The preferred orientation of the grains in these zones is further analyzed, and Figure 7 shows (111) pole figures of the five zones in the FSW joints. The {110} <112> component has a particularly strong intensity of about 10.67 in BM and 10.59 in HAZ. In RS-TMAZ, AS-TAMZ, and SZ, the texture changes, and the intensity gradually decreases from 10.67 to 2.53 compared with BM. The reason is that the probe rotation generates severe plastic deformation in SZ and TMAZ, which can destroy the texture of BM and make the texture rotate along the ND axis.

SEM images of BM and HAZ and EDS results of HAZ are shown in Figure 8. There are small secondary phases in the BM, while the secondary phases in the HAZ are relatively coarse, with a maximum size of about 10 μm. The phase analysis shows that coarse secondary phases have higher copper content, which can be regarded as $\theta$ ($Al_2Cu$) phases. Coarse $\theta$ phases in HAZ are formed by over-aging during heating of the matrix in the FSW process.

### 3.3 Mechanical properties

The hardness of the welded joint is shown in Figure 9, which gradually decreases from the BM (HV147) to the HAZ and then increases in the SZ.

The variations in hardness on the left and right sides of the weld zone are similar. The hardness of SZ is higher than TMAZ because the grains in the weld zone are transformed into equiaxed grains with

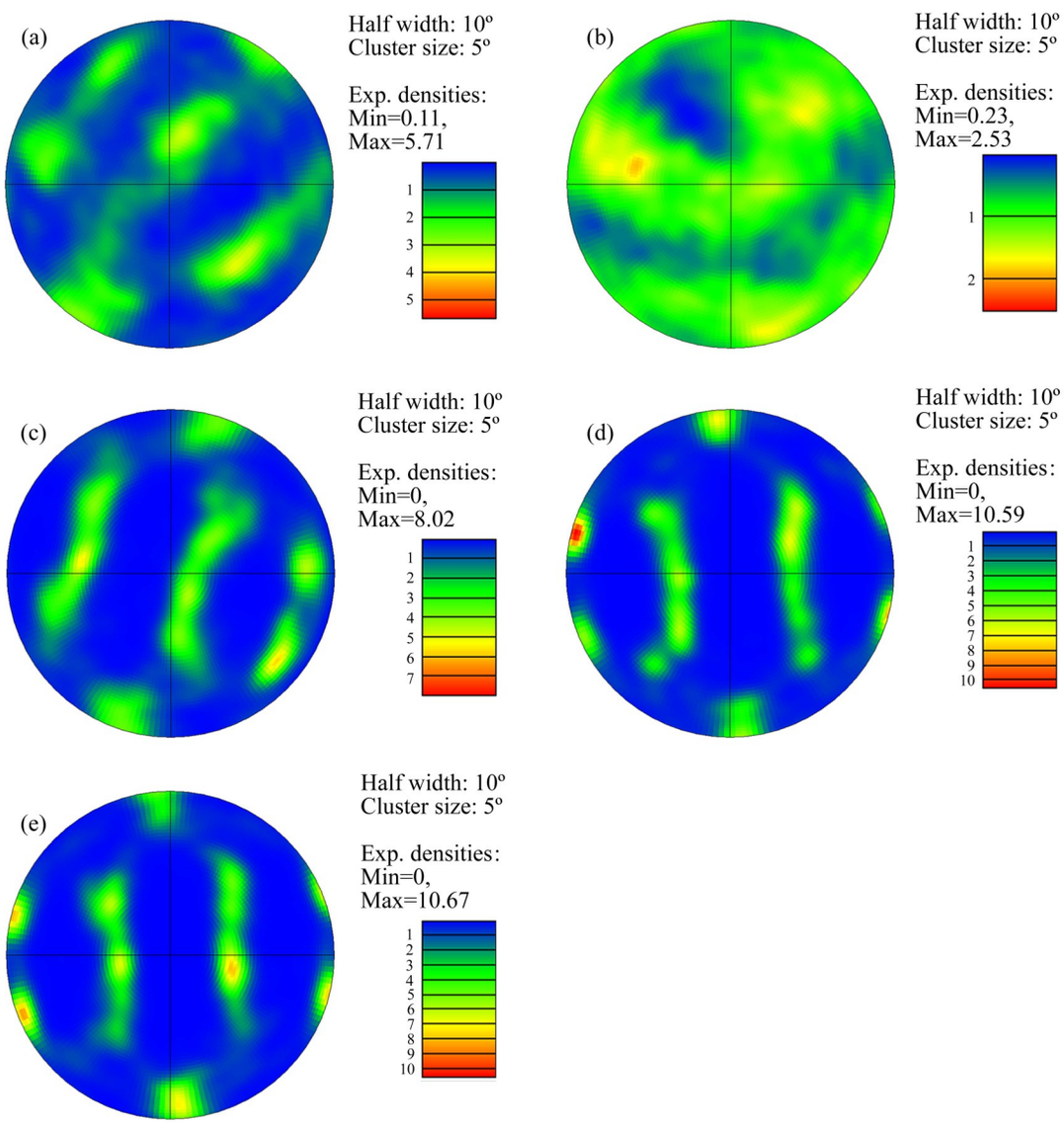


**Figure 7** (111) pole figures of (a) AS-TMAZ, (b) SZ, (c) RS-TMAZ, (d) HAZ and (e) BM of friction stir welding joints

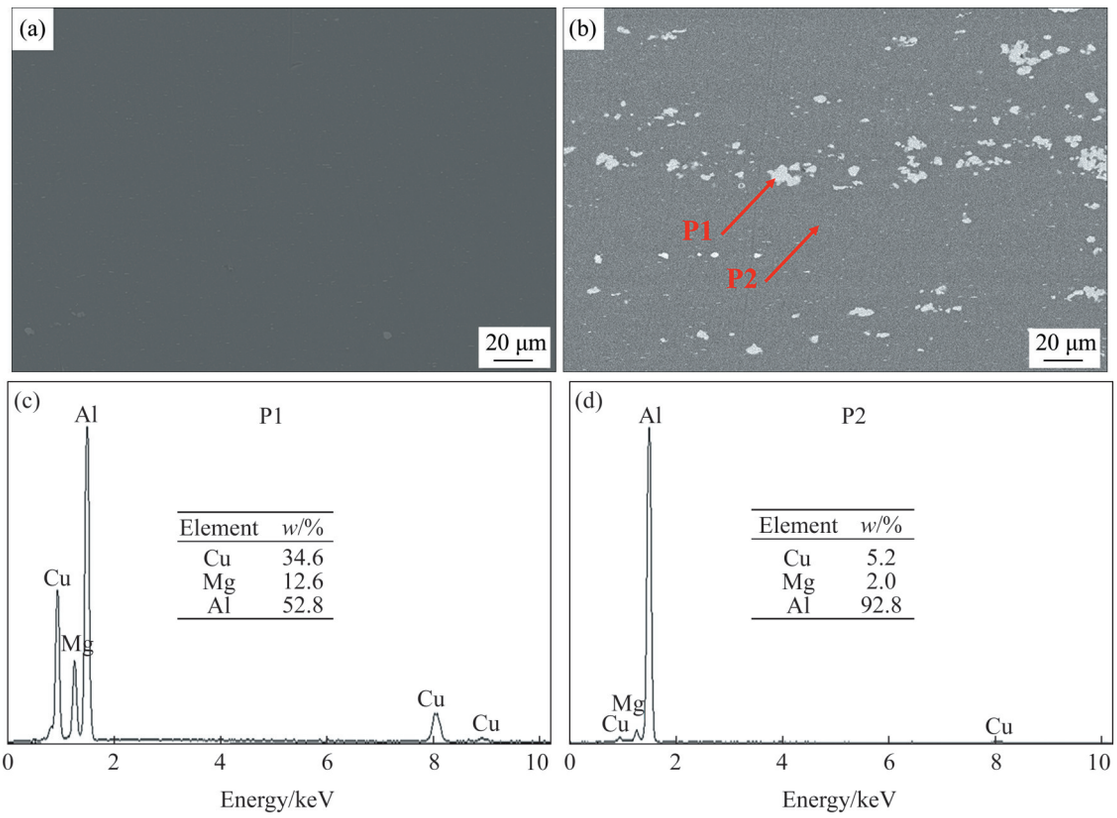


**Figure 8** SEM images of BM (a), HAZ (b) and EDS results of P1 (c) and P2 (d) locations of HAZ

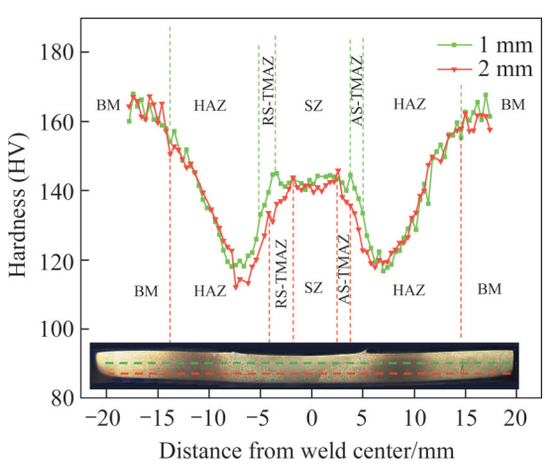


**Figure 9** Microhardness along the friction stir welding joint cross-section 1 mm and 2 mm from top surface

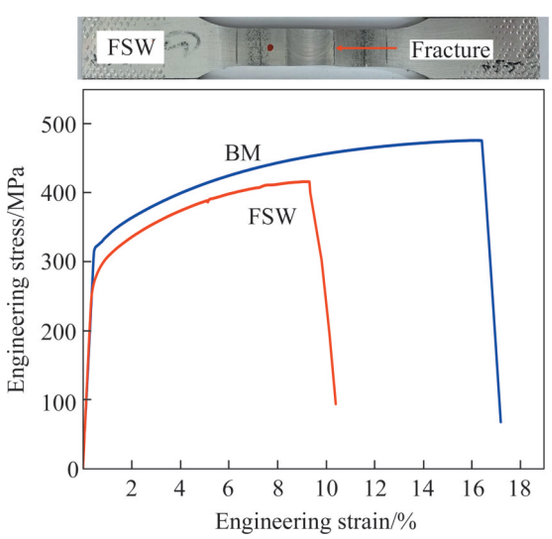


**Figure 10** Room temperature engineering strain vs stress curves of BM and friction stir welding joints

smaller size under thermal cycling and stirring, which has a certain strengthening effect in this zone. Moreover, the hardness of the RS-TMAZ is slightly lower than that of the AS-TMAZ. The HAZ becomes the weakest zone at HV112.3, which is 7 mm from the weld zone. This is due to over-aging from thermal effects of repeated stirring.

Figure 10 shows the engineering strain–stress curves and fracture location of the base material and FSW samples measured at room temperature. The YS and UTS values of the FSW sample are slightly lower than BM. As seen in Figure 10, the welded sample breaks at HAZ, which is consistent with the lowest hardness and the largest grain size of HAZ.

Figure 11 shows the fracture surface of the BM and FSW samples. All fracture surfaces are composed of microporous aggregate fractures, which signifies ductile fracture characteristics.

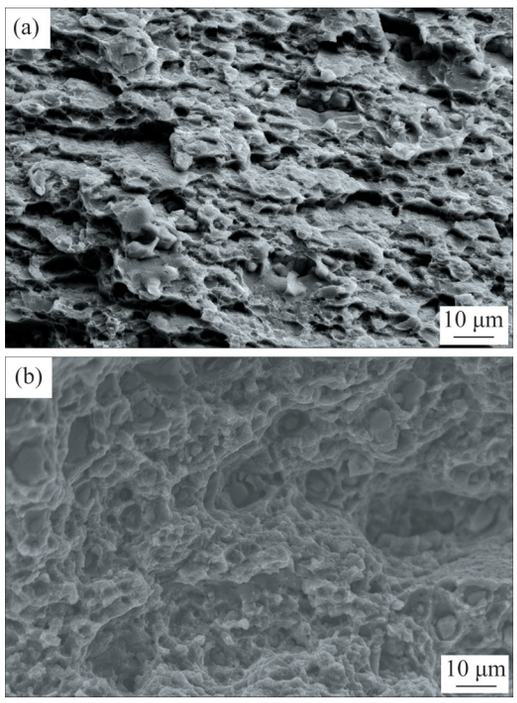


**Figure 11** Fracture surfaces (a) before and (b) after friction stir welding of powder metallurgy AA2024 alloy

Figure 11(a) indicates that many fine dimples can be observed and no secondary phase particles can be found in the BM sample. After the FSW process, the secondary phase particles are found at the bottom of some dimples of the FSW sample in Figure 11(b). The average size of these dimples is less than 5 μm. The secondary phase is the $\theta$ phase by the over-aging behavior of HAZ.

As reported in articles [35 − 37] for polycrystalline materials, grain size strengthening, the Orowan strengthening (including dispersion strengthening and precipitation strengthening), and solution strengthening jointly contribute to the overall yield strength. In this paper, for the sake of simplicity, the authors neglect the solution strengthening for its minute effect. It can be inferred that there are two main reasons for the reduction of HAZ strength. First, the average grain size in the HAZ increases. Second, the cyclic heating in the HAZ leads to precipitated phases growth because of over-aging in connection with the Orowan strengthening. Consequently, the reduction in YS can be calculated using the following equation:

$$\Delta\sigma_{HAZ}=\Delta\sigma_{GS}+\Delta\sigma_{OA} \tag{2}$$

where $\Delta\sigma_{HAZ}$ is the YS reduction of HAZ relative to BM, $\Delta\sigma_{GS}$ is the contribution to the grain growth, and $\Delta\sigma_{OA}$ is the influence of over-aging. The effect of grain size on the YS of metallic materials follows the Hall-Petch relationship:

$$\Delta\sigma_{GS}=k(d_{HAZ}^{-1/2}-d_{BM}^{-1/2}) \tag{3}$$

where $k$ is the Hall-Petch coefficient, $d_{HAZ}$ and $d_{BM}$ are average grain sizes of HAZ and BM, respectively. The average grain sizes, $d_{HAZ}$, and $d_{BM}$, have been calculated from EBSD analysis, 5.03 μm and 4.43 μm, respectively. For wrought aluminum alloy, $k$=0.04 MPa·m$^{1/2}$ [38]. Plugging the values of $d_{HAZ}$, $d_{BM}$, and $k$ in Equation (3), one can get the calculated value of $\Delta\sigma_{GS}$ as −1.2 MPa. The effect of grain growth on the YS in HAZ is feeble.

During over-aging the microstructure evolves with precipitates growth. The associated strengthening can be estimated using the Orowan mechanism:

$$\sigma_{Or}=MGb\frac{\sqrt{f}}{r} \tag{4}$$

where $G$ is the shear modulus; $b$ is the Burgers vector; $M$ is the Taylor factor; $f$ is the volume fraction of precipitated particles; and $r$ is their average radius. As seen in Figure 8(a), the secondary phases in base metal (BM) mainly consist of the nanoscale $\theta'$ and $S'$ phases [39], and a small amount of the $\theta$ phase ($r\leqslant$5 μm). After welding, the $r$ of the secondary phases in the HAZ changes to 5 − 20 μm as seen in Figure 8(b). Accordingly, the enhancement of $r$ reflecting the precipitates growth decreases the $\sigma_{Or}$, resulting in the YS reduction. Regarding the influence of over-aging behavior in the HAZ, it is difficult to carry out a quantitative analysis. However, the $\Delta\sigma_{OA}$ should be negative (−42.8 MPa) because of the decreased strength of the HAZ with the sharp $\Delta\sigma_{GS}$ decrease of 44 MPa, which is the difference in YS values measured by tensile tests between BM and sample 9, as listed in Table 2. Previous studies have demonstrated that the grain growth in HAZ caused by heating during the welding process of PM AA2024 alloy is not obvious, and the reduction in strength is limited. This is because PM aluminum has excellent thermal stability due to the existence of alumina nanoparticles in the matrix, which limits the growth of crystal grains [3]. In this work, the main reason for the decrease in welding performance is over-aging. Table 2 compares the welding performance of

**Table 2** Grain size, joint coefficient and elongation of PM AA2024, DC 2024 and 2014

| Sample | Grain size of BM/μm | Grain size of HAZ/μm | Joint coefficient/% | Elongation/% | Reference |
|---|---|---|---|---|---|
| PM 2024-T4 (FSW) | 4.43 | 5.04 | 85 | 9.5 | This work |
| DC 2024-T8 (FSW) | — | — | 72 | −2.5 | [40] |
| DC 2014-T6 (FSW) | 20 | 50 | 73 | 5.0 | [41] |
| DC 2024-T3 (FSW) | — | — | 75 | 4.1 | [42] |

PM AA2024 and direct casting (DC) 2024. The welding performance of PM AA2024 is better than DC 2024 under the same conditions.

## 4 Conclusions

In this paper, the optimal welding parameters of PM AA2024-T4 plates were obtained, and the microstructure, mechanical properties, and fracture characteristics of FSW joints under the optimal welding parameters were investigated. The conclusions are as follows:

1) The FSW joint of PM AA2024-T4 plate exhibits excellent mechanical properties with the UTS of 415 MPa (85% of the BM strength) and 9.5% elongation after 2000 r/min rotation speed and 100 mm/min traverse speed. Tensile fracture appears in HAZ.

2) The average grain size of the SZ, BM, and HAZ is 2.15 μm, 4.43 μm, and 5.03 μm, respectively. The grains of the BM and HAZ are preferentially oriented along the <110> direction, and a few grains are distributed along the <001> direction. There is no obvious preferred orientation in the TMAZ and SZ.

3) The hardness of the BM is HV147 and the hardness of the FSW joint gradually decreases from BM to HAZ. The lowest value of hardness is about HV112.3, which appears near HAZ.

4) The over-aging behavior caused by repeated heating in HAZ during the welding process is the main reason for the strength decrease of the PM AA2024 after FSW.

## Contributors

HAN Wei-hao and CHEN Cun-guang conducted the literature review and wrote the draft of the manuscript. LI Pei, LIU Nan, DONG Shi-peng, GUO Zhi-meng, YANG Fang and SUI Yan-li analyzed the measured data. CHEN Cun-guang provided the concept and edited the draft of manuscript. VOLINSKY Alex A modified the English language of the manuscript. All authors replied to reviewers' comments and revised the final version.

## Conflict of interest

HAN Wei-hao, LI Pei, LIU Nan, CHEN Cun-guang, DONG Shi-peng, GUO Zhi-meng, YANG Fang, SUI Yan-li and VOLINSKY Alex A. declare that they have no conflict of interest.

## References

[1] HUO Shu-hai, MAIS B. Characteristics of heat resistant nanoquasicrystalline PM aluminum materials [J]. Metal Powder Report, 2017, 72(1): 45 − 50. DOI: 10.1016/j. mprp. 2016.07.003.

[2] STEEDMAN G, BISHOP D P, CALEY W F, et al. Surface porosity investigation of aluminum-silicon PM alloys [J]. Powder Technology, 2012, 226: 225 − 230. DOI: 10.1016/j. powtec.2012.04.049.

[3] CHEN Cun-guang, LI Feng, HAN Wei-hao, et al. Thermally stable Al conductor prepared from Al powder with a low oxygen content [J]. Materials Science and Engineering A, 2021, 813: 141174. DOI: 10.1016/j.msea.2021.141174.

[4] SWEET G A W, AMIRKHIZ B S, WILLIAMS B W, et al. Microstructural evolution of a forged 2xxx series aluminum powder metallurgy alloy [J]. Materials Characterization, 2019, 151: 342−350. DOI: 10.1016/j.matchar.2019.03.033.

[5] WANG Tao, HUANG Yu-feng, YANG Lun, et al. Microstructure and mechanical properties of 7055 Al alloy prepared under different sintering conditions using powder by-products [J]. Materials Science and Engineering A, 2021, 805: 140562. DOI: 10.1016/j.msea.2020.140562.

[6] MANN R E D, HEXEMER R L, DONALDSON I W, et al. Hot deformation of an Al-Cu-Mg Powder metallurgy alloy [J]. Materials Science and Engineering A, 2011, 528(16, 17): 5476−5483. DOI: 10.1016/j.msea.2011.03.081.

[7] BOLAND C D, HEXEMER R L, DONALDSON I W, et al. Industrial processing of a novel Al-Cu-Mg powder metallurgy alloy [J]. Materials Science and Engineering A, 2013, 559: 902−908. DOI: 10.1016/j.msea.2012.09.049.

[8] CHEN Cun-guang, HAN Wei-hao, QI Miao, et al. Microstructural evolution and mechanical properties of an ultrahigh-strength Al-Zn-Mg-Cu alloy via powder metallurgy and hot extrusion [J]. Journal of Central South University, 2021, 28(4): 1195−1205. DOI: 10.1007/s11771-021-4669-y.

[9] REN Jian, WANG Ri-chu, FENG Yan, et al. Microstructure evolution and mechanical properties of an ultrahigh strength Al-Zn-Mg-Cu-Zr-Sc (7055) alloy processed by modified powder hot extrusion with post aging [J]. Vacuum, 2019, 161: 434−442. DOI: 10.1016/j.vacuum.2019.01.013.

[10] HU Lian-xi, LIU Zu-yan, WANG Er-de. Microstructure and mechanical properties of 2024 aluminum alloy consolidated from rapidly solidified alloy powders [J]. Materials Science and Engineering A, 2002, 323(1, 2): 213−217. DOI: 10.1016/S0921-5093(01)01348-X.

[11] GRAYSON G N, SCHAFFER G B, GRIFFITHS J R. Observations of oxide films on fatigue fracture surfaces of a sintered 2xxx series aluminium alloy [J]. Materials Science and Engineering A, 2007, 454−455: 99−103. DOI: 10.1016/j.msea.2006.11.012.

[12] ZHANG Chao, WAN Yang-jie, ZOU Wen-jun, et al. Composition optimization for Al-Zn-Mg-Cu alloys based on thermodynamics and first-principles calculations [J]. Computational and Theoretical Chemistry, 2021, 1201: 113293. DOI: 10.1016/j.comptc.2021.113293.

[13] SO H, WON S J, PARK J, et al. Mechanical properties and microstructural evolution in Al-Cu-Mg-Ag alloy with a $Cu_xMgx/10$ content [J]. Materials Science and Engineering A, 2021, 824: 141573. DOI: 10.1016/j.msea.2021.141573.

[14] GÜLERYÜZ G. Relationship between FSW parameters and hardness of the ferritic steel joints: Modeling and optimization [J]. Vacuum, 2020, 178: 109449. DOI: 10.1016/j.vacuum.2020.109449.

[15] KAUSHIK P, KUMAR DWIVEDI D. Induction preheating in FSW of Al-steel combination [J]. Materials Today: Proceedings, 2021, 46: 1091 − 1095. DOI: 10.1016/j. matpr. 2021.01.438.

[16] RAMANA G V, YELAMASETTI B, VARDHAN T V. Effect of FSW process parameters and tool profile on mechanical properties of AA5082 and AA6061 welds [J]. Materials Today: Proceedings, 2021, 46: 826 − 830. DOI: 10.1016/j.matpr.2020.12.801.

[17] G V R, SANKE N. Evaluation of tensile and microstructure properties of AA2014 and AA7075 FSW weldments developed by HSS-10%Co and WC tools [J]. Materials Today: Proceedings, 2021, 46: 913 − 918. DOI: 10.1016/j.matpr.2021.01.060.

[18] KASAI H, MORISADA Y, FUJII H. Dissimilar FSW of immiscible materials: Steel/magnesium [J]. Materials Science and Engineering A, 2015, 624: 250 − 255. DOI: 10.1016/j.msea.2014.11.060.

[19] MOHAMMADZADEH JAMALIAN H, TAMJIDI ESKANDAR M, CHAMANARA A, et al. An artificial neural network model for multi-pass tool pin varying FSW of AA5086-H34 plates reinforced with $Al_2O_3$ nanoparticles and optimization for tool design insight [J]. CIRP Journal of Manufacturing Science and Technology, 2021, 35: 69 − 79. DOI: 10.1016/j.cirpj.2021.05.007.

[20] EIVANI A R, VAFAEENEZHAD H, JAFARIAN H R, et al. A novel approach to determine residual stress field during FSW of AZ91 Mg alloy using combined smoothed particle hydrodynamics/neuro-fuzzy computations and ultrasonic testing [J]. Journal of Magnesium and Alloys, 2021, 9(4): 1304−1328. DOI: 10.1016/j.jma.2020.11.018.

[21] TIAN Wen-ming, LI Song-mei, CHEN Xin, et al. Intergranular corrosion of spark plasma sintering assembled bimodal grain sized AA7075 aluminum alloys [J]. Corrosion Science, 2016, 107: 211 − 224. DOI: 10.1016/j. corsci. 2016.02.034.

[22] KUMAR N, DAS A, PRASAD S B. An analysis of friction stir welding (FSW) of metal matrix composites (MMCs) [J]. Materials Today: Proceedings, 2020, 26: 2650 − 2656. DOI: 10.1016/j.matpr.2020.02.558.

[23] NARENTHIRAN B, PARANTHAMAN P. Investigations on effect of FSW process parameter on hybrid Al MMC using Taguchi approach [J]. Materials Today: Proceedings, 2021, 37: 759−763. DOI: 10.1016/j.matpr.2020.05.787.

[24] SACHINKUMAR, NARENDRANATH S, CHAKRADHAR D. Effect of FSW on microstructure and hardness of AA6061/SiC/fly ash MMCs [J]. Materials Today: Proceedings, 2018, 5(9): 17866−17872. DOI: 10.1016/j.matpr.2018.06.113.

[25] TAO Xi-chen, CHANG Yong-qin, GUO Yuan-hang, et al. Microstructure and mechanical properties of friction stir welded oxide dispersion strengthened AA6063 aluminum matrix composites enhanced by post-weld heat treatment [J]. Materials Science and Engineering A, 2018, 725: 19 − 27. DOI: 10.1016/j.msea.2018.03.094.

[26] CHEN Cun-guang, WANG Wen-wen, GUO Zhi-meng, et al. Annealing effects on microstructure and mechanical properties of ultrafine-grained Al composites reinforced with nano-$Al_2O_3$ by rotary swaging [J]. Journal of Materials Engineering and Performance, 2018, 27(4): 1738 − 1745. DOI: 10.1007/s11665-018-3301-2.

[27] SERCOMBE T B, SCHAFFER G B. On the role of magnesium and nitrogen in the infiltration of aluminium by aluminium for rapid prototyping applications [J]. Acta Materialia, 2004, 52(10): 3019 − 3025. DOI: 10.1016/j.actamat.2004.03.004.

[28] AVETTAND-FÈNOËL M N, SIMAR A, SHABADI R, et al. Characterization of oxide dispersion strengthened copper based materials developed by friction stir processing [J]. Materials & Design, 2014, 60: 343 − 357. DOI: 10.1016/j.matdes.2014.04.012.

[29] BREWER L N, BENNETT M S, BAKER B W, et al. Characterization of residual stress as a function of friction stir welding parameters in oxide dispersion strengthened (ODS) steel MA956 [J]. Materials Science and Engineering A, 2015, 647: 313−321. DOI: 10.1016/j.msea.2015.09.020.

[30] BALOG M, OROVCIK L, NAGY S, et al. To what extent does friction-stir welding deteriorate the properties of powder metallurgy Al? [J]. Journal of Materials Research and Technology, 2020, 9(3): 6733 − 6744. DOI: 10.1016/j.jmrt.2020.04.087.

[31] NOSKO M, ŠTEPÁNEK M, ZIFČÁK P, et al. Solid-state joining of powder metallurgy Al-$Al_2O_3$ nanocomposites via friction-stir welding: Effects of powder particle size on the weldability, microstructure, and mechanical property [J]. Materials Science and Engineering A, 2019, 754: 190 − 204. DOI: 10.1016/j.msea.2019.03.074.

[32] KHODABAKHSHI F, YAZDABADI H G, KOKABI A H, et al. Friction stir welding of a P/M Al-$Al_2O_3$ nanocomposite: Microstructure and mechanical properties [J]. Materials Science and Engineering A, 2013, 585: 222 − 232. DOI:

10.1016/j.msea.2013.07.062.
[33] WANG Tao, YANG Lun, TANG Zhao-feng, et al. Effect of aging treatment on microstructure, mechanical and corrosion properties of 7055 aluminum alloy prepared using powder by-product [J]. Materials Science and Engineering A, 2021, 822: 141606. DOI: 10.1016/j.msea.2021.141606.
[34] WANG Tao, HUANG Yu-feng, YANG Lun, et al. Microstructure and mechanical properties of 7055 Al alloy prepared under different sintering conditions using powder by-products [J]. Materials Science and Engineering A, 2021, 805: 140562. DOI: 10.1016/j.msea.2020.140562.
[35] SHANMUGASUNDARAM T, HEILMAIER M, MURTY B S, et al. On the Hall-Petch relationship in a nanostructured Al-Cu alloy [J]. Materials Science and Engineering A, 2010, 527(29, 30): 7821−7825. DOI: 10.1016/j.msea.2010.08.070.
[36] HUANG Tian-lin, SHUAI Lin-fei, WAKEEL A, et al. Strengthening mechanisms and Hall-Petch stress of ultrafine grained Al-0.3%Cu [J]. Acta Materialia, 2018, 156: 369−378. DOI: 10.1016/j.actamat.2018.07.006.
[37] HANSEN N. Hall-Petch relation and boundary strengthening [J]. Scripta Materialia, 2004, 51(8): 801−806. DOI: 10.1016/j.scriptamat.2004.06.002.
[38] TAN Qi-yang, ZHANG Jing-qi, SUN Qiang, et al. Inoculation treatment of an additively manufactured 2024 aluminium alloy with titanium nanoparticles [J]. Acta Materialia, 2020, 196: 1−16. DOI: 10.1016/j.actamat.2020.06.026.
[39] BADINI C, MARINO F, VERNÉ E. Calorimetric study on precipitation path in 2024 alloy and its SiC composite [J]. Materials Science and Engineering A, 1995, 191(1, 2): 185−191. DOI: 10.1016/0921-5093(94)09637-C.
[40] YOUSEFI SHIVYARI S, HOSSEINI MONAZZAH A. Study on the balance between FSW parameters and heat treatment for an optimized Al2024-T8 joint: Microstructural and tensile evaluations [J]. Production Engineering, 2021, 15(5): 595−603. DOI: 10.1007/s11740-021-01054-2.
[41] MUHAMMAD W, HUSAIN W, TAUQIR A, et al. Assessment of microstructure and mechanical properties of friction stir welded AA2014-O and AA2014-T6 sheets [J]. The International Journal of Advanced Manufacturing Technology, 2021, 115(7, 8): 2255−2267. DOI: 10.1007/s00170-021-07249-2.
[42] YADAV V K, GAUR V, SINGH I V. Effect of post-weld heat treatment on mechanical properties and fatigue crack growth rate in welded AA-2024 [J]. Materials Science and Engineering A, 2020, 779: 139116. DOI: 10.1016/j.msea.2020.139116.

**(Edited by HE Yun-bin)**

## 中文导读

### 粉末冶金AA2024合金搅拌摩擦焊的组织和力学性能

**摘要：**本文通过搅拌摩擦焊(FSW)成功实现了粉末冶金AA2024铝合金挤压板材的焊接，在航空航天、汽车工业领域具有重要应用前景。为了确定FSW的最佳加工参数，对FSW接头的微观结构、力学性能和断裂行为进行研究。结果表明，当搅拌速度为2000 r/min、焊接速度为100 mm/min时，获得最优焊接接头性能，其抗拉强度、屈服强度和伸长率分别为415 MPa(母材强度的85%)、282 MPa和9.5%。焊接接头的硬度从合金基体到热影响区逐渐降低。由于FSW过程中反复搅拌产生热量，样品发生过时效，导致热影响区附近的强度和硬度最低。搅拌区的平均晶粒尺寸(2.15 μm)小于母材(4.43 μm)和热影响区(5.03 μm)，并且热影响区晶粒具有<110>择优取向。

**关键词：**高强度铝合金；粉末冶金；AA2024；搅拌摩擦焊；力学性能